An Improved Series-Connected Hybrid Valve Based on Diode Rectifier Units and Full-Bridge MMC for Large-Scale Offshore Wind Power Transmission

Chengdong Wang[1], Guorong Zhang[1], Jian Zhang[1], Bao Xie[1], and Yong Shi[1]

[1]Hefei University of Technology

December 3, 2022

Abstract

An improved hybrid valve based on diode rectifier units (DRUs) and full-bridge MMC (FB-MMC) to transmit large scale offshore wind power to onshore is proposed to balance the performance and cost of pure DRU- or MMC-based schemes. Approximate one third of DC voltage is constructed by the FB-MMC and the remaining by DRUs. Active power-DC voltage droop control is proposed to regulate the DC voltage of FB-MMC to adaptively transmit the offshore wind farm active power to onshore. Meanwhile, the reactive power consumed by DRUs and generated by wind turbine converters (WTCs) is dynamically balanced by the FB-MMC. During start-up of offshore wind farm, the DC link capacitors of WTCs and auxiliary systems can be energized from onshore. And most importantly, DC pole-to-pole short circuit fault can be ridden-through as quickly as possible by the reverse and double DC voltage of FB-MMC with no severe submodule (SM) capacitor overvoltage after fault occurrence. The system performance is investigated by time-domain simulations in PSCAD/EMTDC. Thus, the feasibility of the proposed scheme is verified.

Hosted file

`An Improved Series-Connected Hybrid Valve Based on Diode Rectifier Units and Full-Bridge MMC for Large S` available at https://authorea.com/users/562276/articles/609622-an-improved-series-connected-hybrid-valve-based-on-diode-rectifier-units-and-full-bridge-mmc-for-large-scale-offshore-wind-power-transmission

Hosted file

`Figure300dpi.rar` available at https://authorea.com/users/562276/articles/609622-an-improved-series-connected-hybrid-valve-based-on-diode-rectifier-units-and-full-bridge-mmc-for-large-scale-offshore-wind-power-transmission

An Improved Series-Connected Hybrid Valve Based on Diode Rectifier Units and Full-Bridge MMC for Large-Scale Offshore Wind Power Transmission

Chengdong Wang [1*], Guorong Zhang [1], Jian Zhang [1], Xie Bao [1], Yong Shi [1]

[1] School of Electrical Engineering and Automation, Hefei University of Technology, Hefei, China
[*] mikeclinton@163.com

Abstract: An improved hybrid valve based on diode rectifier units (DRUs) and full-bridge MMC (FB-MMC) to transmit large scale offshore wind power to onshore is proposed to balance the performance and cost of pure DRU- or MMC-based schemes. Approximate one third of DC voltage is constructed by the FB-MMC and the remaining by DRUs. Active power-DC voltage droop control is proposed to regulate the DC voltage of FB-MMC to adaptively transmit the offshore wind farm active power to onshore. Meanwhile, the reactive power consumed by DRUs and generated by wind turbine converters (WTCs) is dynamically balanced by the FB-MMC. During start-up of offshore wind farm, the DC link capacitors of WTCs and auxiliary systems can be energized from onshore. And most importantly, DC pole-to-pole short circuit fault can be ridden-through as quickly as possible by the reverse and double DC voltage of FB-MMC with no severe submodule (SM) capacitor overvoltage after fault occurrence. The system performance is investigated by time-domain simulations in PSCAD/EMTDC. Thus, the feasibility of the proposed scheme is verified.

Nomenclature

T_{dr}	Linking transformer turn ratio
R_{DC}	DC transmission line resistance
X_T	Equivalent reactance of cables and transformer leakage reactance
K_{dr}	Number of 12-pulse rectifiers
U_{dcnom}^{mmc}	Nominal DC voltage of FB-MMC
P_{nom}^{mmc}	Nominal power of FB-MMC
K_x, T_x	The proportional coefficient and integral time constant of DC voltage controller, reactive power controller, current controller, voltage controller, phase-locked loop controller, and active power controller when x equals to dc, q, i, v, l, and p
K_f	The proportional coefficient of frequency controller
K_{qf}	Reactive power-frequency droop coefficient
R_{eq}, L_{eq}	Equivalent resistance and reactance of FB-MMC
C	SM capacitance
N_1, N_2, N_{on}	SM number in one arm
ω	Angular frequency
s	Laplace operator
K_{ov}^{dc}	DC side overvoltage index, set to 1.2 in this paper
U_{dc}^{r}	The rectifier side (sending side) average DC voltage
U_{dc}^{dr}	The average DRU DC side voltage
U_{dc0}^{dr}	Ideal no-load DRU DC voltage
U_{dc}^{mmc}	The FB-MMC steady state DC side voltage
U_{dc}^{i}	The inverter side (receiving side) steady state DC voltage
I_{DC}	Steady state DC current
U_{POI_RMS}, u_{POI}	Phase RMS and instantaneous voltage of point of interconnection
i_{aPOI}	Phase a instantaneous current of point of interconnection
P_{dc}^{r}, P_{dc}^{i}	The sending and receiving side DC power
P_g	Total active power of offshore wind farm
P_{mmc}	AC side power of FB-MMC
P_{dr}	AC side power of DRUs
P_{dc}^{mmc}	MMC DC side power
P_{dc}^{dr}, $P_{dc\_RMS}^{dr}$	DRUs DC side power and its RMS value
u_{dcref}^{mmc}	FB-MMC DC voltage reference
u_{dc}^{mmc}	Instantaneous FB-MMC DC voltage
u_{dc}^{dr}, $u_{dc\_RMS}^{dr}$	Instantaneous DRUs voltage and its RMS value
u_{dc}^{r}, $u_{dc\_RMS}^{r}$	Instantaneous rectifier end DC voltage and its RMS value
u_{dc}^{i}	Instantaneous inverter end DC voltage
i_{dc}^{r}, i_{dc}^{i}	The rectifier and inverter DC current
I_{POI}	Instantaneous current of point of interconnection
m_0, m	Droop coefficient
I_{dref}^{mmc}, I_{d}^{mmc}	d-axis components of the FB-MMC current reference and feedback value
I_{qref}^{mmc}, I_{q}^{mmc}	q-axis components of the FB-MMC current reference and feedback value
u_{d}^{POI}, u_{q}^{POI}	d- and q-axis components of POI voltage
$u_{ddiffref}^{mmc}$, $u_{qdiffref}^{mmc}$	d- and q-axis components of differential modulation quantities
u_{CY}^{X}	Y (Y = T, B) arm SM capacitor voltage of phase X (X = A, B, C)
u_{CYR}^{X}	Y (Y = T, B) arm redundant SM capacitor voltage of phase X (X = A, B, C)
Q_{dr}, Q_g, Q_{mmc}	Reactive power of DRUs, offshore wind farm and FB-MMC
i_{dc}	Instantaneous DC current
m_a, m_{2a}, m_{max}	Fundamental, second harmonic and maximal modulation index
θ, θ_2	Fundamental and second harmonic initial phase angle
i_{cir}	Circulating current

I_m	AC current magnitude
$u_{cx}^{\sum y}$	Sum arm x (x = l or u) SM capacitor voltage of phase y (y = a, b, or c)
S_{yx}	Arm x equivalent switch function of phase y
φ	Power factor of DRUs
μ	Overlap angle
K	Root locus gain
k	Proportional gain of droop coefficient generation controller

1. Introduction

Nowadays, renewable energy plays more and more critical roles in energy pattern transition to realize net zero emission for all the globe. By the end of 2020, more than 707 GW cumulative photovoltaic capacity and up to 743 GW global cumulative wind power, including 34 GW offshore wind, have been installed [1], [2]. However, since the mismatch distribution of energy resources and power loads in some countries, the high voltage alternate current (HVAC) and high voltage direct current (HVDC) power transmission technologies have been intensively developed and immense projects have been in commission. Line-commutated converter-based HVDC (LCC-HVDC) and voltage-source converter-based HVDC (VSC-HVDC) have been the main stream of HVDC technology for onshore bulk power transmission [3]. Since the topology of modular multilevel converter (MMC) was proposed in 2003 [4], for the merits of modularity and scalability, low harmonic and easy construction for high voltage, intensive investigations [5]-[14] have been conducted, and many an MMC-HVDC transmission project has been deployed and planed in European Union, United Kingdom, China and United States for renewable energy integration application. Literature [15] has shown that the HVDC transmission is advantageous in long distance transmission and large-scale offshore wind power application due to the reduction of power loss, transmission corridors and submarine cables [16].

In fact, MMC-HVDC-based offshore wind power has been attracting increasingly more interest for its reduced acoustic and visual impact on humans [17]-[19] and strong and steady sea wind, which means offshore WTCs own much larger capacity, thus yielding more power compared with onshore WTCs, whereas imposing difficulty in collection and transmission link due to insulation of submarine cables. Compared with LCC-HVDC, MMC-HVDC has been being the preferred choice for connecting offshore wind farms (OWFs) because it can establish a strong voltage for individual WTC grid access. However, the MMC-HVDC transmission for offshore wind power also faces great challenges because the offshore application brings critical demands in volume and weight for the offshore converter. When the capacity reaches giga watt scale, the offshore platform is so bulky that building and transporting a platform like this is a costly and hard task, which may hinder the offshore wind power exploitation. For this reason, diode rectifier unit-based high voltage direct current (DRU-HVDC) transmission, as shown in Fig. 1, was proposed for its remarkable reduction in volume and weight for the elimination of a large number of DC capacitors compared with MMC, consequently saving installation and

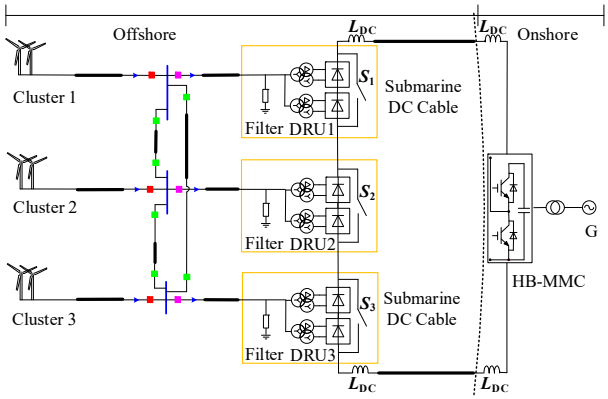

Fig. 1. *System configuration in [22]*

maintenance time and costs and cutting down transmission loss by twenty percent [20].

However, the DRU rectifier has its own disadvantages.

1) It has no controllability of AC voltage amplitude and frequency of point of connection (POI), resulting in complicated and coupled control strategy of individual WTCs in different clusters. A triple closed loop active power control and quad closed loop reactive power and phase-locked loop-based (PLL) frequency control strategy [21], [22] in synchronous rotating frame (dq frame) was proposed to coordinate individual grid side converters (GSCs) to establish AC collection system voltage and frequency. In this scheme, the control loop parameter tuning and stability analysis become extremely difficult compared with onshore wind power, so the frequency and reactive power control is performed just by proportional controller, which may introduce static error and turn into a problem in an isolated collection system encompassing hundreds of GSCs without self-synchronization capability like synchronous generator. In [23]-[25], a distributed voltage and frequency control strategy initially proposed to adapt to LCC-HVDC onshore converter was successfully implemented using a VSC-HVDC converter model by changes in the control of machine side converters (MSCs) in order to provide grid forming capability for the GSCs. However, the measurement and communication of POI voltage to all the wind power converters is necessary, which may deteriorate its performance in large scale offshore wind power because of enormous communication substations and time delay. Another problem is that it may not be applicable to doubly-fed induction generators (DFIGs) for lacking in grid voltage at starting up stage. In [26], a global positioning system-based (GPS) fixed reference frame in dq frame is put forward to generate a phase angle reference for GSCs to replace the conventional PLL for type 3 wind generators and permanent magnetic synchronous generators (PMSGs, also known as type 4 wind generators). In essence, it is an open loop frequency control and the performance directly depends on the reliability of GPS signal source, which may malfunction in harsh sea circumstances.
2) It cannot actively regulate transmission power. The characteristic of DRU is adversely to regulate transmission power real-time because the transformer

leakage reactance voltage drop increases with DC current increasing, consequently decreasing the sending terminal DC voltage, and vice versa, whereas the DRU cannot regulate its DC terminal voltage by itself except for adjusting AC terminal voltage by WTCs. In [21], [22], the DRU AC terminal voltage is controlled indirectly by individual GSCs in closed loop form coordinately.

3) Dynamic reactive power compensation is necessary. Theoretically, reactive power consumed by a 12-pulse DRU completely depends on the overlap angle given that the DC current is constant [5]. As the active power varies with wind speed, the reactive power varies simultaneously. In [21], a distributed reactive power control strategy was proposed. Just as analyzed above, the reactive power is open loop controlled as the fourth target and need to be transmitted to the POI (DRU terminal) by AC collection cables. In [26], a combination scheme of capacitor banks and three phase AC umbilical cables linked to POI with AC/AC conversion is proposed to dynamically transmit reactive power from onshore, which increases the costs of the transmission system.

4) It cannot supply the energy for offshore network during start-up and maintenance. In [21], [22], it is assumed that there is energy storage installed at some WTs to provide self-startup capability. In [26], three phase AC umbilical cables are used to start-up the unidirectional DRU-HVDC-based OWFs.

5) It cannot block the DC short circuit fault current. In [27], a short circuit current transferring thyristor is parallel connected to the FB-MMC to protect it, and the AC side circuit breaker also switches off in DC pole-to-pole fault.

In [27], a series-connected DRU and FB-MMC topology is proposed, in which the active power is regulated by a proportional and integral controller that is not applicable to a sending valve for offshore wind power transmission because the OWF active power is stochastic and varying. Meanwhile, the DC voltage of FB-MMC is only 165 kV with 1100 kV overall DC voltage, so that the reverse FB-MMC DC voltage when blocked is too small to be utilized to block DC short circuit current because of severe overvoltage of FB-MMC SM capacitors. In addition, transformers are equipped for the FB-MMC and reactive power compensator and harmonic filter are also necessary for DRU rectifier.

In this paper, an improved series-connected DRU and FB-MMC topology is proposed to transmit large-scale offshore wind power to onshore, in which approximate two thirds of sending end DC voltage are constructed by DRU units and approximate one third by FB-MMC. The transformer for FB-MMC and the compensator and harmonic filter for DRU are unnecessary. The analysis is based on the offshore wind power scenario, considering that the output characteristic of converter is different from that of ideal voltage source in [27]. The main contributions are as follows.

1) Active power-DC voltage droop control strategy is proposed so that the transmission power can be adaptively regulated corresponding to total wind active power, by which the controllability of overall offshore network is enhanced. The stability range of droop coefficient is investigated and the dynamical droop coefficient determination is given to balance the power of FB-MMC and DRUs.

2) The dynamical reactive power control strategy is proposed to balance the reactive power consumed by the DRUs and that generated by submarine cable distributed capacitors and filters of each GSCs. Therefore, a large-scale offshore wind farm with a huge number of cables can be constructed and operated at different power level.

3) The ride-through process of DC pole-to-pole short circuit fault is analyzed, which is an obstacle for DRU-based scheme. By cancelling the DRU DC voltage with reverse and double DC voltage of FB-MMC when blocked without switching off the AC breaker, the DC short circuit current can be suppressed to around zero as quickly as possible so as to enhance the fault response performance.

4) The precharged scheme is given to energize DC link capacitors of WTCs and auxiliary systems before power transmission.

The remainder of this paper is organized as follows. Section II depicts the overall integration and transmission configuration. In Section III, the power regulation principle and control strategy are analyzed and investigated in detail; subsequently, the reactive power is assessed by analytical calculation to conform the reactive power balance capability among wind farms, DRUs and FB-MMC; finally, DC bus pole-to-pole fault ride-though capability, and start-up procedure is illustrated. In Section IV, the simulation results verify the feasibility of the proposed configuration and the corresponding control strategy. Section V presents the discussion and conclusion.

2. System description

The system configuration with 66 kV AC collection cable voltage is shown in Fig. 2. Each DRU unit consists of two 12-pulse uncontrolled rectifiers, two Y/y/d11 linking transformers, and one thyristor switch. A small capacity three phase FB-MMC is series connected in DC side to produce approximate one third of the DC bus voltage. And its AC side is directly connected to POI, which means reactive power compensation capacitor banks and one third of transformers are cut down. The FBSM is adopted to attain the capability of blocking DC side pole-to-pole short circuit current from the offshore side, which implies the leakage reactance of DRU transformers could be smaller. Meanwhile, the FB-MMC can charge the offshore network

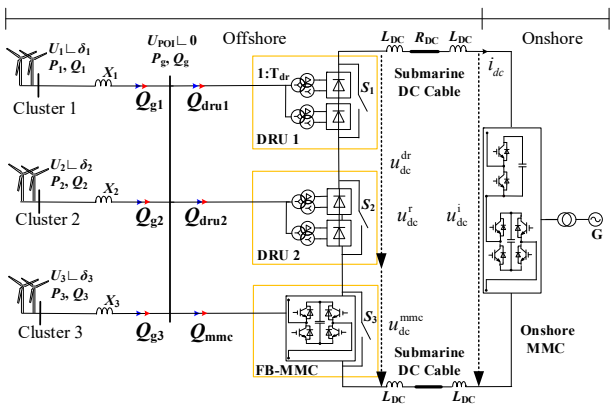

Fig. 2. System configuration diagram

and GSCs DC link capacitors during start-up and maintenance by closing the DRU thyristor switches S1 and S2 and switching off its AC side breakers.

3. System control

3.1. Control of the Wind Turbine Converter

As analyzed in [21], [22], given that the DRU unit is uncontrolled rectifier, the offshore network AC voltage amplitude, frequency, and phase are established by the GSCs through d-and q-axis control loop by which the output voltage of GSCs (i.e., filter capacitor voltage) is controlled by adjusting the filter inductor current. Therefore, the POI voltage is established by all GSCs through AC collection cable distributed resistors, inductors, and capacitors. In this paper, the reactive power reference is set to zero so that the GSCs could operate in approximate unit power factor. Control of MSCs remains the same as [21], [22], that is to say, the DC link voltage is controlled at constant in q-axis and d-axis current reference is set to zero if there is no need to regulate generator flux linkage.

3.2. Analysis and Control of the FB-MMC

The analysis in [21], [22] has shown that transmission power positively depends on the POI voltage magnitude, which means when the wind power increases, the magnitude of GSCs output voltage increases, thus the magnitude of POI voltage increases, and vice versa. However, the DC voltage comprises two parts for the hybrid valve. The principle is analyzed in detail as follows.

3.2.1. Power Regulation Principle and Control Strategy

The circuit of dc-link is depicted in Fig. 2. In steady state, according to Kirchhoff voltage law, the dc-link voltage can be expressed as follows:

$$U_{\mathrm{dc}}^{\mathrm{r}} = U_{\mathrm{dc}}^{\mathrm{dr}} + U_{\mathrm{dc}}^{\mathrm{mmc}} = R_{\mathrm{DC}} I_{\mathrm{DC}} + U_{\mathrm{dc}}^{\mathrm{i}} \tag{1}$$

$$U_{\mathrm{dc}}^{\mathrm{dr}} = 2K_{\mathrm{dr}}\left(3\sqrt{6}U_{\mathrm{POI}}T_{\mathrm{dr}}/\pi - 3X_{\mathrm{T}}I_{\mathrm{DC}}/\pi\right) \tag{2}$$

Thus, the transmission power determined by the POI voltage at the sending side can be expressed as follows.

$$\begin{aligned} P_{\mathrm{dc}}^{\mathrm{r}} = {} & \frac{R_{\mathrm{DC}}}{\left(6K_{\mathrm{dr}}X_{\mathrm{T}}/\pi + R_{\mathrm{DC}}\right)^2}\left(6\sqrt{6}K_{\mathrm{dr}}U_{\mathrm{POI}}T_{\mathrm{dr}}/\pi + U_{\mathrm{dc}}^{\mathrm{mmc}}\right)^2 \\ & + \frac{6K_{\mathrm{dr}}X_{\mathrm{T}}/\pi - R_{\mathrm{DC}}}{\left(6K_{\mathrm{dr}}X_{\mathrm{T}}/\pi + R_{\mathrm{DC}}\right)^2}\left(6\sqrt{6}K_{\mathrm{dr}}U_{\mathrm{POI}}T_{\mathrm{dr}}/\pi + U_{\mathrm{dc}}^{\mathrm{mmc}}\right)U_{\mathrm{dc}}^{\mathrm{i}} \\ & - \frac{6K_{\mathrm{dr}}X_{\mathrm{T}}/\pi}{\left(6K_{\mathrm{dr}}X_{\mathrm{T}}/\pi + R_{\mathrm{DC}}\right)^2}\left(U_{\mathrm{dc}}^{\mathrm{i}}\right)^2 \end{aligned} \tag{3}$$

It can be clearly revealed that the transmission power is a quadratic function of POI voltage and only when the no-load sending side voltage is larger than the receiving side voltage can power be transmitted to onshore side. In [21], [22], this no-load sending side voltage is determined by the POI voltage by setting K_{dr} to 6 and $U_{\mathrm{dc}}^{\mathrm{mmc}}$ to 0, whereas by setting K_{dr} to 4 and $U_{\mathrm{dc}}^{\mathrm{mmc}}$ to a proper value in this paper.

Meanwhile, after the POI voltage increases to the starting voltage, $U_{\mathrm{POI}}^{\mathrm{start}}$, expressed as

$$U_{\mathrm{POI}}^{\mathrm{start}} = \left(U_{\mathrm{dc}}^{\mathrm{i}} - U_{\mathrm{dc}}^{\mathrm{mmc}}\right)\Big/\left(6\sqrt{6}K_{\mathrm{dr}}/\pi\right), \tag{4}$$

the transmission power is significantly affected by the equivalent transformer leakage reactance, which is smaller in this paper than that in [21], [22] owing to the FB-MMC fault current blocking capability, implying that the transmission power is boosted with the same POI voltage.

Based on the above observation, a FB-MMC DC voltage droop control is proposed to adaptively regulate the offshore wind power as

$$u_{\mathrm{dcref}}^{\mathrm{mmc}} = U_{\mathrm{dcnom}}^{\mathrm{mmc}} - m\left(P_{\mathrm{nom}}^{\mathrm{mmc}} - P_{\mathrm{g}}/3\right), \tag{5}$$

and

$$P_{\mathrm{g}} = P_{\mathrm{mmc}} + P_{\mathrm{dr}}. \tag{6}$$

$U_{\mathrm{dcnom}}^{\mathrm{mmc}}$ and $P_{\mathrm{nom}}^{\mathrm{mmc}}$ equal to one third of corresponding total nominal value of sending side respectively. The active power- DC voltage droop relationship is illustrated in Fig. 3.

From (4) and (5), the initial droop coefficient can be set by the starting voltage as

$$m = \left(6\sqrt{6}U_{\mathrm{POI}}^{\mathrm{start}}K_{\mathrm{dr}}/\pi - U_{\mathrm{dc}}^{\mathrm{i}} + U_{\mathrm{dcnom}}^{\mathrm{mmc}}\right)\Big/\left(P_{\mathrm{nom}}^{\mathrm{mmc}} - P_{\mathrm{g}}/3\right), \tag{7}$$

and the loop stability will be analyzed in the following subsection.

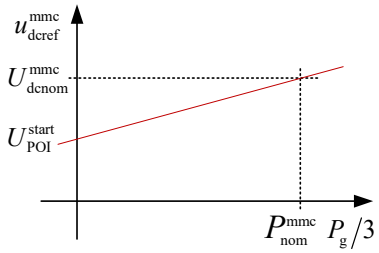

Fig. 3. *Active power-DC voltage droop curve*

3.2.2. Stability Analysis of DC Voltage Droop Control

Fig. 4 shows the overall control diagram. The d-axis of FB-MMC control is oriented on POI phase voltage, that is to say, the q-axis component of POI phase voltage is input of the FB-MMC PLL. The circulating current control is still based on negative sequence DQ frame rotating with two times angular frequency.

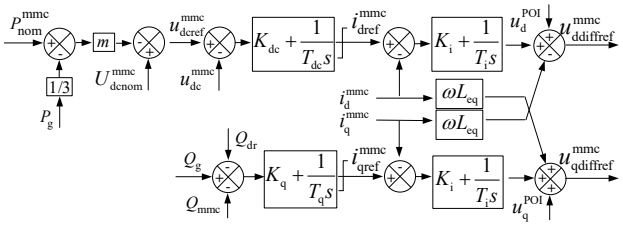

Fig. 4. *Control diagram of FB-MMC differential*

To obtain droop coefficient *m*, the DC voltage loop could be modeled as follows. With the internal- and inter-arm submodule voltage balance algorithm, all the submodule voltages could be considered identical. For low frequency components, the lower and upper arm equivalent switch function could be expressed as

$$\begin{aligned} S_{\mathrm{al}} &= 0.5+0.5m_{\mathrm{a}}\cos(\omega t+\theta)+m_{2\mathrm{a}}\cos(2\omega t+\theta_2)\\ S_{\mathrm{bl}} &= 0.5+0.5m_{\mathrm{a}}\cos(\omega t+\theta-2\pi/3)+m_{2\mathrm{a}}\cos(2\omega t+\theta_2+2\pi/3)\\ S_{\mathrm{cl}} &= 0.5+0.5m_{\mathrm{a}}\cos(\omega t+\theta+2\pi/3)+m_{2\mathrm{a}}\cos(2\omega t+\theta_2-2\pi/3) \end{aligned} \tag{8}$$

and

$$\begin{aligned} S_{\mathrm{au}} &= 0.5-0.5m_{\mathrm{a}}\cos(\omega t+\theta)+m_{2\mathrm{a}}\cos(2\omega t+\theta_2)\\ S_{\mathrm{bu}} &= 0.5-0.5m_{\mathrm{a}}\cos(\omega t+\theta-2\pi/3)+m_{2\mathrm{a}}\cos(2\omega t+\theta_2+2\pi/3)\\ S_{\mathrm{cu}} &= 0.5-0.5m_{\mathrm{a}}\cos(\omega t+\theta+2\pi/3)+m_{2\mathrm{a}}\cos(2\omega t+\theta_2-2\pi/3) \end{aligned} \tag{9}$$

If the AC currents are written as

$$\begin{aligned} i_{\mathrm{a}} &= I_{\mathrm{m}}\cos(\omega t)\\ i_{\mathrm{b}} &= I_{\mathrm{m}}\cos(\omega t-2\pi/3),\\ i_{\mathrm{c}} &= I_{\mathrm{m}}\cos(\omega t+2\pi/3) \end{aligned} \tag{10}$$

the following relationship could be obtained for each arm

$$\begin{aligned} \frac{C}{N}\frac{du_{\mathrm{cl}}^{\sum\mathrm{a}}}{dt} &= -S_{\mathrm{al}}\left(-\frac{i_{\mathrm{a}}}{2}+i_{\mathrm{cir}}\right)\\ \frac{C}{N}\frac{du_{\mathrm{cl}}^{\sum\mathrm{b}}}{dt} &= -S_{\mathrm{bl}}\left(-\frac{i_{\mathrm{b}}}{2}+i_{\mathrm{cir}}\right)\\ \frac{C}{N}\frac{du_{\mathrm{cl}}^{\sum\mathrm{c}}}{dt} &= -S_{\mathrm{cl}}\left(-\frac{i_{\mathrm{c}}}{2}+i_{\mathrm{cir}}\right) \end{aligned} \tag{11}$$

$$\begin{aligned} \frac{C}{N}\frac{du_{\mathrm{cu}}^{\sum\mathrm{a}}}{dt} &= -S_{\mathrm{au}}\left(\frac{i_{\mathrm{a}}}{2}+i_{\mathrm{cir}}\right)\\ \frac{C}{N}\frac{du_{\mathrm{cu}}^{\sum\mathrm{b}}}{dt} &= -S_{\mathrm{bu}}\left(\frac{i_{\mathrm{b}}}{2}+i_{\mathrm{cir}}\right)\\ \frac{C}{N}\frac{du_{\mathrm{cu}}^{\sum\mathrm{c}}}{dt} &= -S_{\mathrm{cu}}\left(\frac{i_{\mathrm{c}}}{2}+i_{\mathrm{cir}}\right) \end{aligned} \tag{12}$$

With circulating current control, the second harmonic current is controlled to zero, therefore circulating current is mainly composed of DC current. On the other hand, because the harmonic components of the six sum arm capacitor voltages are symmetry and the DC voltage component from the coupling effect of SM capacitor harmonic voltages and switching function AC components are negligible small, the average of sum arm capacitor voltages can be replaced by the DC voltage, $u_{\mathrm{dc}}^{\mathrm{mmc}}$, to obtain

$$6\frac{C}{N}\frac{du_{\mathrm{dc}}^{\mathrm{mmc}}}{dt} = 0.75m_{\mathrm{a}}I_{\mathrm{m}}\cos(\theta)-i_{\mathrm{dc}}. \tag{13}$$

According to the definition of equivalent switch function and AC current, θ is the angle between the output voltage vector and output current vector, so it can be concluded that

$$i_{\mathrm{d}}^{\mathrm{mmc}} = I_{\mathrm{m}}\cos(\theta). \tag{14}$$

With the above analysis, the active power control loop can be expressed as Fig. 5.

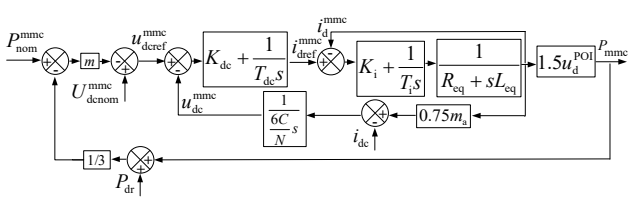

Fig. 5. *Active power control loop*

It is obvious that the active power control loop is a triple closed loop, so the stability analysis is necessary. From Fig. 5, the closed loop transfer function of active power control can be expressed as

$$P_{\mathrm{mmc}} = \frac{G_1}{1+G_1}P_{\mathrm{nom}}^{\mathrm{mmc}}+\frac{G_2}{1+G_2}U_{\mathrm{dcnom}}^{\mathrm{mmc}}+\frac{G_3}{1+G_3}P_{\mathrm{dr}}+\frac{G_4}{1+G_4}i_{\mathrm{dc}} \tag{15}$$

where

$$\begin{aligned} G_1 &= \frac{-m\frac{6C}{N}sA}{\left(1+\frac{2}{3}mA\right)\frac{6C}{N}s+\frac{A}{2m_{\mathrm{a}}u_{\mathrm{d}}^{\mathrm{POI}}}}\\ G_2 &= \frac{\frac{6C}{N}sA}{\left(1-\frac{1}{3}mA-A\right)\frac{6C}{N}s+\frac{A}{2m_{\mathrm{a}}u_{\mathrm{d}}^{\mathrm{POI}}}}\\ G_3 &= \frac{\frac{m}{3}\frac{6C}{N}sA}{\left(1-\frac{2}{3}mA\right)\frac{6C}{N}s+\frac{A}{2m_{\mathrm{a}}u_{\mathrm{d}}^{\mathrm{POI}}}}\\ G_4 &= \frac{A}{\left(1-\frac{1}{3}mA\right)\frac{6C}{N}s+\frac{A}{2m_{\mathrm{a}}u_{\mathrm{d}}^{\mathrm{POI}}}-A} \end{aligned} \tag{16}$$

and

$$A = \frac{1.5u_{\mathrm{d}}^{\mathrm{POI}}\left(K_{\mathrm{dc}}T_{\mathrm{dc}}s+1\right)\left(K_{\mathrm{i}}T_{\mathrm{i}}s+1\right)}{T_{\mathrm{dc}}s\left(T_{\mathrm{i}}L_{\mathrm{eq}}s^2+T_{\mathrm{i}}\left(R_{\mathrm{eq}}+K_{\mathrm{i}}\right)s+1\right)}. \tag{17}$$

By proper transformation, the characteristic equation can be obtained as

$$1+\frac{-3m\frac{C}{N}u_{\mathrm{d}}^{\mathrm{POI}}\left(K_{\mathrm{dc}}T_{\mathrm{dc}}s+1\right)\left(K_{\mathrm{i}}T_{\mathrm{i}}s+1\right)s}{as^4+bs^3+cs^2+ds+e} = 0 \tag{18}$$

where

$$a=6\frac{C}{N}T_{\mathrm{dc}}T_{\mathrm{i}}L_{\mathrm{eq}},\quad b=6\frac{C}{N}T_{\mathrm{dc}}T_{\mathrm{i}}\left(R_{\mathrm{eq}}+K_{\mathrm{i}}\right),$$

$$c=6\frac{C}{N}T_{\mathrm{dc}}+\frac{3K_{\mathrm{dc}}T_{\mathrm{dc}}K_{\mathrm{i}}T_{\mathrm{i}}}{4m_a},\quad d=\frac{3\left(K_{\mathrm{i}}T_{\mathrm{i}}+K_{\mathrm{dc}}T_{\mathrm{dc}}\right)}{4m_a},\quad e=\frac{3}{4m_a}.$$

It can be clearly revealed that the root locus of active power closed loop is a negative gain root locus, and the root locus varies with different fundamental modulation index, m_{a}, corresponding to different operation point. To obtain the range of droop coefficient which stabilize the hybrid rectifier valve, root loci under different modulation indices

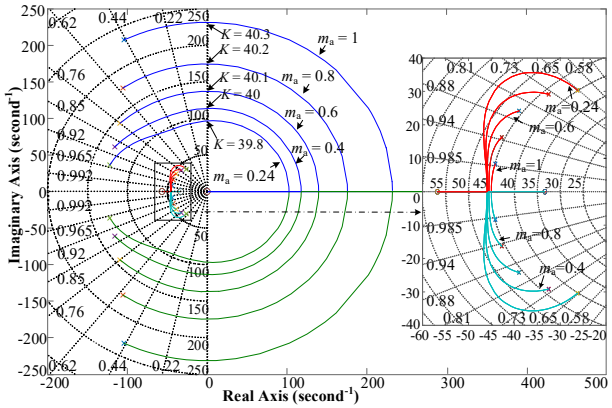

Fig. 6. *Root loci*

Table 1 Parameter of tested system

Components	Parameters	Values
HVDC link	Power	DRUs 800 MW FB-MMC 400 MW
	DC voltage	DRUs 426 kV FB-MMC 214 kV
12-pulse Diode Rectifier	Transformer (Y/Y/Δ)	66/174.6/174.6 kV
	Leakage inductance	0.08/0.08/0 pu
FB-MMC	Submodule capacitance	10 mF
	Submodule number per arm N_1	107
	Redundancy submodule number per arm N_2	10
	Submodule capacitor voltage	2 kV
	Arm inductance	29 mH
Onshore MMC	Submodule capacitance	10 mF
	Submodule number per arm N_{on}	320
	Submodule capacitor voltage	2 kV
	Arm inductance	29 mH
	Transformer (Y/Δ)	380/220 kV
	Leakage reactance	0.18 pu
DC Cables	Length	200 km
Smoothing Reactor	L_{SM}	0.03 H
GSC Converters	Rating of individual WT	1.5 kV/5 MW
	Rating of a WT cluster	600 MW
	Transformer (Y/Δ)	0.69/66 kV
	Leakage inductance	0.08 pu
	Filter capacitor	0.1 pu
	Filter resistance	0 pu
	Filter reactance	0.15 pu
	Switching frequency	1.95 kHz
	AC cable length	10 km; 10 km
FB-MMC Control Parameters (pu)	Current control: K_i; T_i	0.48; 0.0367
	Q control: K_q; T_q	0.48; 0.0367
	DC voltage control: K_{dc}; T_{dc}	1.5; 0.02
Onshore MMC Control Parameters (pu)	Current control: K_i; T_i	0.48; 0.0067
	Q control: K_q; T_q	0.48; 0.0303
	DC voltage control: K_{dc}; T_{dc}	8.0; 0.00267
GSC Control Parameters (pu)	Current control: K_i; T_i	6.63; 3.04e-4
	Voltage control: K_v; T_v	0.33; 6.40e-3
	PLL: K_l; T_l	0.23; 8.059e-5
	P control: K_p; T_p	0.2; 0.002
	f control: K_f	0.08864
	Q-f droop control: K_{qf}	0.1

are shown in Fig. 6 with parameters listed in Table I.

It is obvious that the product of droop coefficient and POI voltage indicated by root locus gain, K, in above figure gets the minimum stability range when the fundamental modulation index reaches its minimum value. On the basis of power regulation principle of the last subsection, the minimum modulation index appears when the FB-MMC DC voltage reaches its maximum with a zero DC current scenario. According to (1) and (2), with FB-MMC DC overvoltage limit K_{ov}^{dc}, the minimal modulation index can be obtained as 0.24. So, the stability range can be acquired from the root loci as

$$mu_d^{POI} < 39.8 \quad . \tag{19}$$

3.2.3. Active Power Balance and Dynamical Droop Coefficient Determination

From the active power control loop in Fig. 5, it can be seen that the active power of DRUs is a disturbance term for the FB-MMC control. However, the active power of DRUs cannot be actively controlled. So, the power balance strategy is necessary to avoid the power and DC voltage imbalance between the DRUs and FB-MMC. For the series connection of DC side, the active power can be chosen as an indicator, and a proportional controller is added to dynamically modify the droop coefficient. The initial droop coefficient, m_0, can be set to 0.2 for a good damping from Fig. 6. To avoid FB-MMC and DRUs DC side overvoltage, the droop coefficient must be constrained in a proper range. If DRUs DC overvoltage limit is K_{ov}^{dc}, the maximal FB-MMC DC voltage variation can be obtained as

$$\Delta U_{dc} = (K_{ov}^{dc} - 1)(\frac{2}{3}U_{dc}^{r}) \tag{20}$$

, and the dynamical droop coefficient upper limit can be determined as

$$m_{max} = \begin{cases} \dfrac{\Delta U_{dc}}{\left| P_{nom}^{mmc} - P_g/3 \right|} & P_{nom}^{mmc} \neq P_g/3 \\ m_0 & P_{nom}^{mmc} = P_g/3 \end{cases} \quad . \tag{21}$$

Therefore, the dynamical droop coefficient generation procedure can be given as Fig. 7.

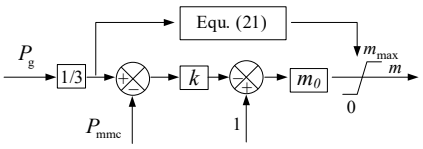

Fig. 7. *Droop coefficient generation*

The proportional gain, k, can be designed considering the most power imbalance scenario. From Fig. 6, when the FB-MMC power reaches its upper limit indicated by K_{ov}^{dc}, the droop coefficient should be assigned to 0.51 to gain the optimized damping with the product value 15.7 of droop coefficient and POI voltage under the fundamental modulation index 0.24. Thus, the proportional gain can be expressed as

$$k = \frac{1.55}{(K_{ov}^{dc} - 1)P_{nom}^{mmc}} \quad . \tag{22}$$

3.2.4. Reactive Power Control

In LCC-HVDC-based onshore wind farm integration and transmission application, the capacitor banks are usually

adopted to compensate reactive power. However, in recent years, there are a lot of reports on the overvoltage fault caused by slow dynamical response of reactive power compensation. In DRU-based offshore wind farm integration [21], [22], the reactive power of DRUs and WTs are still balanced by capacitor banks. In this paper, the series-connected FB-MMC can be utilized to dynamically balance the reactive power of DRUs and WTs, which can further decrease the volume and weight of offshore platform.

The reactive power required for 12-pulse DRUs during operation can be assessed as follows [5]

$$Q_{\mathrm{dr}} = P_{\mathrm{dr}} \tan\varphi \tag{23}$$

$$\tan\varphi = \frac{(\pi/180)\mu - \sin\mu\cos\mu}{\sin^2\mu} \tag{24}$$

$$\mu = \cos^{-1}[U_{\mathrm{dc}}^{\mathrm{dr}}/U_{\mathrm{dc0}}^{\mathrm{dr}} - (X_{\mathrm{T}}/\sqrt{2})(I_{\mathrm{d}}/(U_{\mathrm{POI}}T_{\mathrm{dr}}))] \tag{25}$$

Therefore, the maximal reactive power requirement can be acquired under the situation that the active power of DRUs reaches its maximum, that is, the DC voltage of DRUs reaches its maximum with the overvoltage limit, $K_{\mathrm{ov}}^{\mathrm{dc}}$.

Based on the above analysis, the reactive power control strategy is given in Fig. 4. By the proportional integral controller which operates as static reactive power compensator, the rapidity of reactive power response is achieved in contrast to capacitor banks.

3.2.5. DC Pole-to-Pole Short Circuit Blocking Capability Analysis

In [28], a combined DC fault protection scheme is proposed by restricting onshore FB-MMC DC current and providing q-axis current of individual GSCs for restarting the transmission. However, the short circuit DC current may be very large if DC smoothing reactance and transformer leakage reactance is not large enough. In this paper, at fault detection stage, the DC current from sending side is increasing rapidly, thus the DC side overcurrent protection is triggered timely by blocking the FB-MMC. Subsequently, the FB-MMC DC voltage reverses because the DC short circuit current flows through antiparallel diodes. With all SMs, including redundant SMs, blocked, the FB-MMC DC voltage steps to more than two times its current value and surpasses the DRUs DC voltage so that the DC short circuit current decreases and decays to zero, implying that the power output of GSCs is interrupted. When DC short circuit fault is cleared, the FB-MMC is deblocked and then transmission recovers. With the active power balance control, the DRUs DC voltage is almost two times the FB-MMC DC voltage when pole-to-pole short circuit fault occurs, so the voltage between DC cable short circuit points is relatively small because the DC side voltage of DRUs is cancelled by the FB-MMC DC side voltage, as shown in Fig. 8. With the FB-MMC arm reactors and DC smoothing reactors, the transient DC fault current is acceptedly small for semiconductor devices and cables. Meanwhile, the DC fault current coming from onshore side is restricted by DC bus smoothing reactor and inverse voltage of FBSMs of onshore MMC.

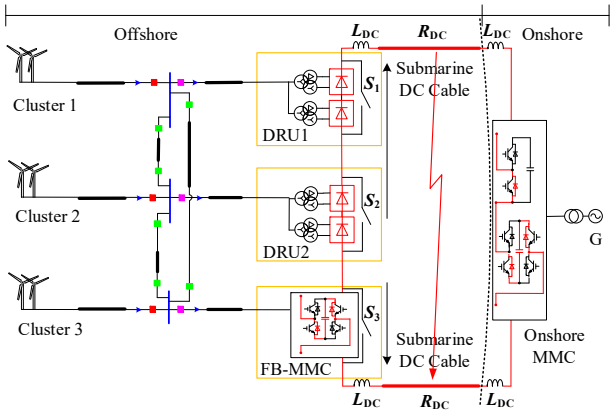

Fig. 8. *DC short circuit loop*

3.2.6. Start-up Control

Just as aforementioned in Section I, the start-up of offshore wind farm needs to charge DC link capacitors of WTCs and auxiliary systems. In this paper, the FB-MMC can be utilized to fulfill this requirement with control strategy, by which offshore network voltage and frequency are controlled by the FB-MMC and DC bus voltage is controlled by onshore MMC and set to be one third of rated value, i.e., the rated FB-MMC DC voltage. At this stage, the upper and lower arm output voltage of onshore MMC could be negative, so the number of HBSM and FBSM must be designed carefully so as to restrict fault current and reduce losses and cost simultaneously.

4. Time-domain simulations

A simulation model of the proposed system is built in PS CAD/EMTDC for the performance validation as shown in Fig. 9. Parameters are already listed in Table I. As in [21], the DC side of WTCs is considered as an ideal DC source. Two equivalent wind turbines are both rated at 600 MW, that is to say, the output current is 120 times individual WTC. The DRU is composed of 12 diodes from PSCAD master library and the FB-MMC and onshore MMC model is from sample case DCS1_Released_20140630. The onshore MMC and transformer capacity is both 1200 MVA.

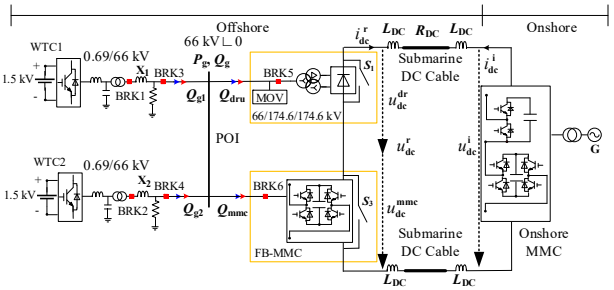

Fig. 9. *Simulation model for the offshore windfarm integration system*

4.1. Start-up Performance

During start-up, the onshore MMC operates in DC voltage control mode referenced to 213 kV and reactive power

control mode referenced to 400 MW, respectively. The FB-MMC operates in islanded mode with 66 kV line voltage magnitude and 50 Hz frequency reference respectively. The start-up waveforms are illustrated in Fig. 10. At t = 0.01 s, the onshore MMC is deblocked, and then DC bus voltage is rapidly established with all FB-MMC capacitors charged to half nominal voltage simultaneously. At t = 0.5 s, the FB-MMC is deblocked and the nominal POI voltage is established smoothly with the SM capacitor voltage reaching its nominal value, which means the WTCs DC link capacitors and auxiliary systems, such as uninterruptable power supply for the control system and lights, can be charged to start the offshore wind farm.

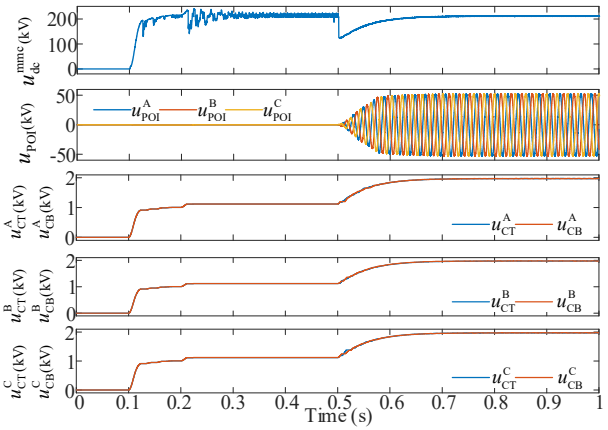

Fig. 10. *Start-up waveforms, including FB-MMC DC side voltage, AC side voltage, and three phase SM capacitor voltage*

4.2. Power Regulation Performance

Fig. 11 illustrates the system response to power regulation. It is assumed that the WTCs DC link capacitors and auxilia ry systems have already been charged before 0 s. The system start-up procedure is listed in Table II.

As can be seen from Fig. 11(c), the POI voltage is kept at 40 kV as set for GSCs to synchronize before 3.4 s. At 3.4 s, with FB-MMC deblocked, the active power references start to clamp smoothly and reach rated value at 6 s. At 7 s, the active power references step to 0.9 pu and maintain for 1 second and then restore to 1 pu at 8 s. From 9 s, the active power references step to 1.1 pu and maintain for 1 second and then restore to 1 pu at 10 s. Fig. 11(a) and (b) shows the power and voltage waveforms. It can be clearly observed

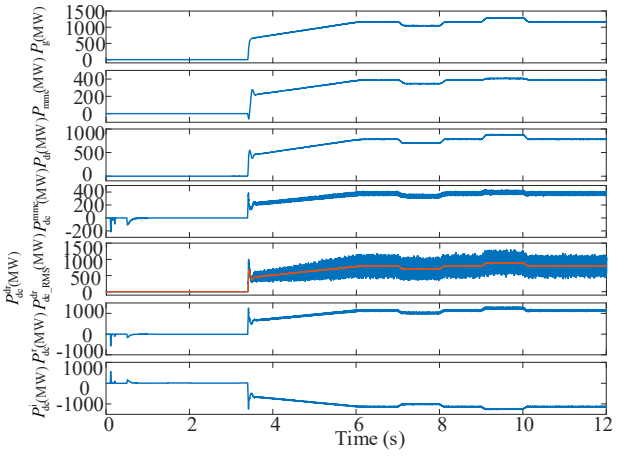

a

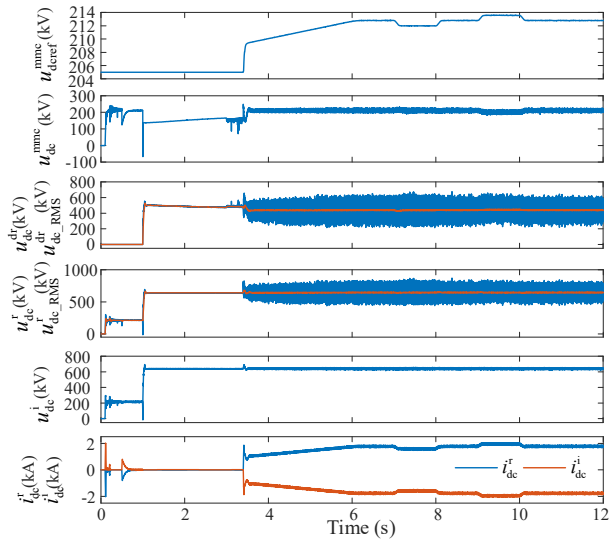

b

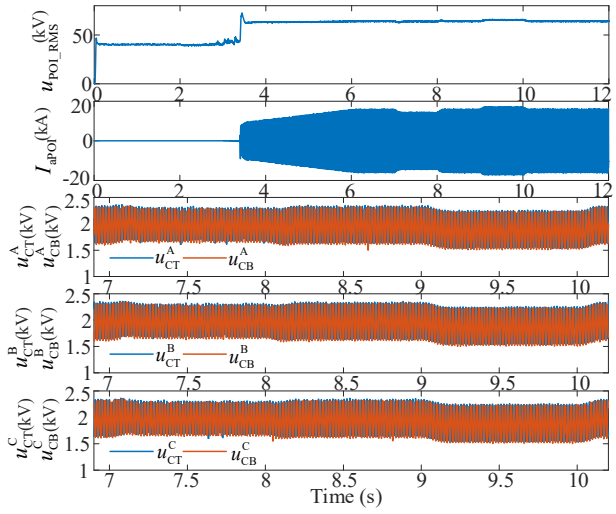

c

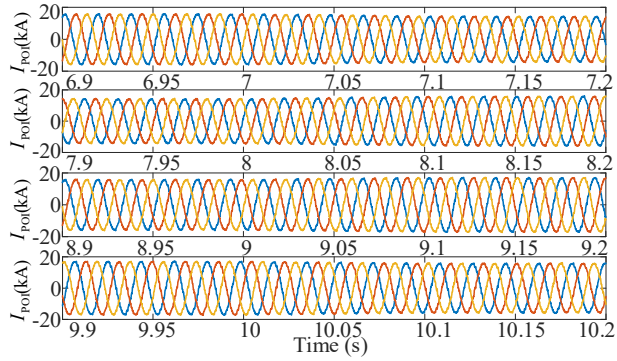

d

Fig. 11. *Power regulation waveforms, including (a) total wind farm active power Pg, FB-MMC active power Pmmc, DRUs active power Pdr, FB-MMC DC side voltage P_{dc}^{mmc}, DRUs DC side voltage P_{dc}^{dr} and its RMS value $P_{dc\_RMS}^{dr}$, total sending side power P_{dc}^{r}, and total receiving side power P_{dc}^{i}, and (b) FB-MMC DC voltage reference u_{dcref}^{mmc}, FB-MMC DC voltage u_{dc}^{mmc}, DRUs DC side voltage u_{dc}^{dr} and its RMS value $u_{dc\_RMS}^{dr}$, total sending side DC voltage u_{dc}^{r} and its RMS value $u_{dc\_RMS}^{r}$, receiving side DC voltage u_{dc}^{i}, sending side DC current i_{dc}^{r} and receiving side DC current i_{dc}^{i}, (c) POI voltage RMS value uPOI_RMS, total POI current phase A iaPOI, and FB-MMC three phase SM capacitor voltage u_{CT}^{A}, u_{CB}^{A}, u_{CT}^{B}, u_{CB}^{B}, u_{CT}^{C}, u_{CB}^{C}, and (d) total POI current during regulation.*

Table 2 System start-up procedure

Time	Events
0	Simulation starts
10 ms	BRK1 and BRK3 (seen in Fig. 10) are closed and WTC1 is deblocked with voltage set to 0.6 pu and active power control set to proportional mode
1 s	BRK2 and BRK4 are closed and synchronization of WTC2 starts
2 s	WTC2 is deblocked with voltage set to 0.6 pu and active power control set to proportional mode
3 s	BRK5 and BRK6 are closed and synchronization of FB-MMC starts
3.4 s	FB-MMC is deblocked and power references of WTC1 and WTC2 start to clamp at 1 pu/s until 1 pu with power control set to proportional-integral mode and voltages start to increase at 0.4 pu/s until 1 pu
7 s	Power references of WTC1 and WTC2 step to 0.9 pu
8 s	Power references of WTC1 and WTC2 restore to 1 pu
9 s	Power references of WTC1 and WTC2 step to 1.1 pu
10 s	Power references of WTC1 and WTC2 restore to 1 pu

that the FB-MMC DC voltage reference varies corresponding to the power under approximate 12 ms response time with no overshoot. Although the FB-MMC DC side voltage decreases slightly at 9 s, the power shared by FB-MMC still rises because the DC current increases with total wind farm active power rising. Seeing that the DC side voltage and power of DRUs varies severely, the RMS values are also plotted to make a contrast with that of FB-MMC. Fig. 11(c) shows the SM capacitor voltages still keep well balanced whether the total wind farm power decreases or increases. And the total wind farm current is shown in Fig. 11(d). Finally, it can be concluded that the DC voltage and power are well shared between DRUs and FB-MMC.

4.3. Reactive Power Balance Performance

The reactive power of wind farm, DRUs and FB-MMC under power regulation condition and fault condition is depicted in Fig. 12. It can be clearly concluded that a) the total wind farm reactive power and DRUs reactive power varies positively corresponding to wind farm active power, and b) the reactive power is well balanced under both conditions and the total wind farm reactive power is kept at a lower level such that the wind farm power factor approximates one.

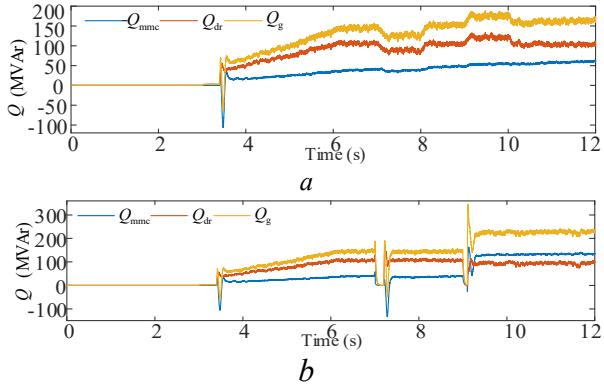

Fig. 12. *Reactive power waveforms of (a) power regulation condition and (b) fault condition*

4.4. Fault Ride-Through Performance

The DC pole-to-pole short circuit fault and offshore AC fault ride-through performance are verified in Fig. 13.

At 7 s, the DC bus pole-to-pole short circuit fault is triggered and the DC current rises rapidly to the DC overcurrent threshold 4 kA. After fault detection time of 40 us, all SMs are blocked and then the DC current steps to zero. After 200 ms, the fault is cleared and the system begins to restore. Although there exist spikes of DC power when fault occurs and restores, the DRUs and FB-MMC does not show severe overvoltage in AC and DC side. The SM capacitor voltages, including redundant SMs inserted to elevate reverse DC voltage to suppress DC fault current, rise to 3 kV at most compared with rated value 2 kV.

At 9 s, the three phase phase-to-ground fault at offshore POI bus is triggered. As soon as the lowest instantaneous value of the three phase voltage decreases to the undervoltage threshold of 0.1 pu, the FB-MMC is blocked. With the DC voltage being kept at rated value of 640 kV by onshore MMC, the transmission power attenuates rapidly to 0 MW. After 100 ms, the fault is cleared and POI voltage and transmission power restores to rated value with

reasonable overshoot of POI voltage and DRUs DC side voltage. During fault, the total current of wind farm just rises slightly as shown in Fig. 13(d).

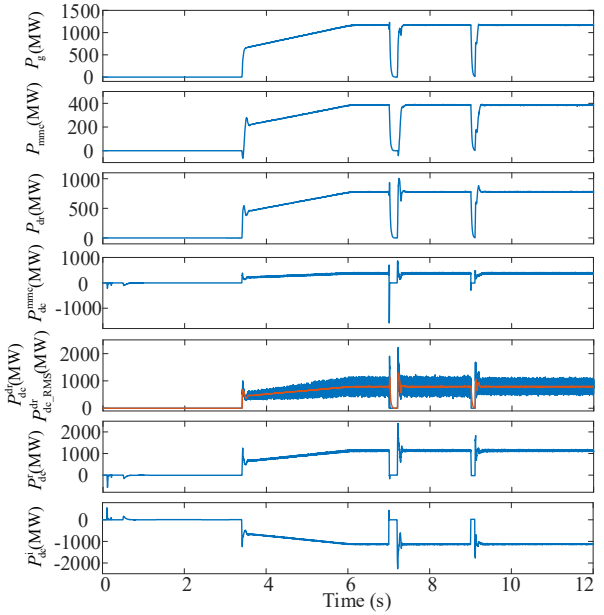

a

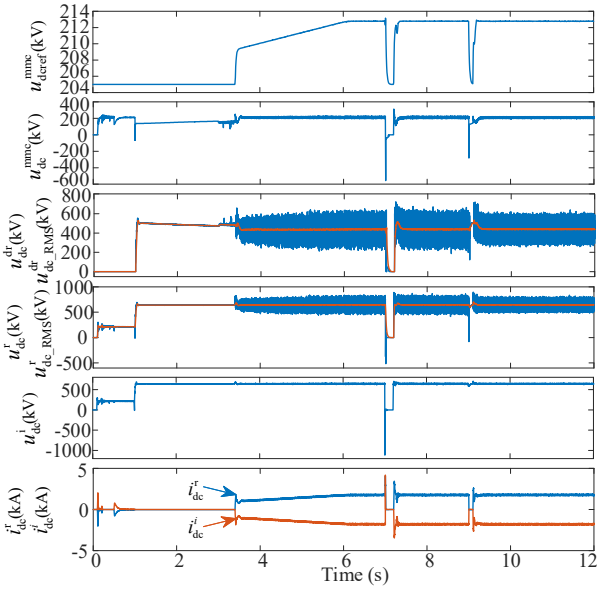

b

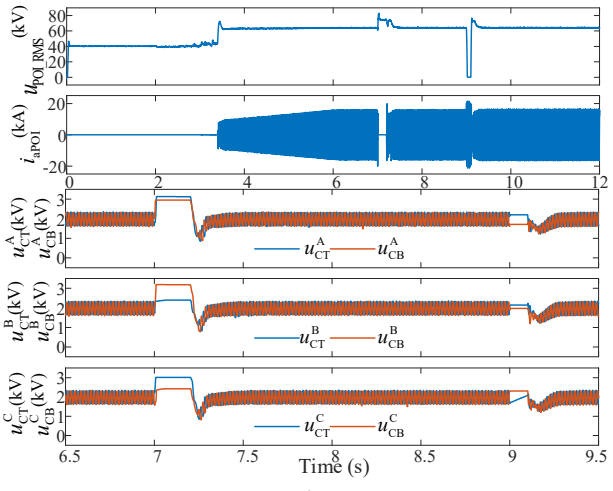

c

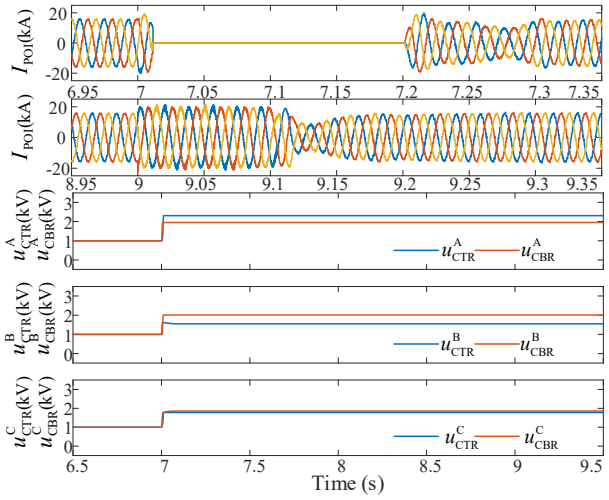

d

Fig. 13. *Fault ride-through waveforms, including (a) total wind farm active power P_g, FB-MMC active power P_{mmc}, DRUs active power P_{dr}, FB-MMC DC side voltage P_{dc}^{mmc}, DRUs DC side voltage P_{dc}^{dr} and its RMS value $P_{dc\_RMS}^{dr}$, total sending side power P_{dc}^{r}, and total receiving side power P_{dc}^{i}, and (b) FB-MMC DC voltage reference u_{dcref}^{mmc}, FB-MMC DC voltage u_{dc}^{mmc}, DRUs DC side voltage u_{dc}^{dr} and its RMS value $u_{dc\_RMS}^{dr}$, total sending side DC voltage u_{dc}^{r} and its RMS value $u_{dc\_RMS}^{r}$, receiving side DC voltage u_{dc}^{i}, sending side DC current i_{dc}^{r} and receiving side DC current i_{dc}^{i}, (c) POI voltage RMS value u_{POI_RMS}, total POI current phase A i_{aPOI}, and FB-MMC three phase SM capacitor voltage u_{CT}^{A}, u_{CB}^{A}, u_{CT}^{B}, u_{CB}^{B}, u_{CT}^{C}, u_{CB}^{C}, and (d) total POI current I_{POI} and redundant SM voltage u_{CTR}^{A}, u_{CBR}^{A}, u_{CTR}^{B}, u_{CBR}^{B}, u_{CTR}^{C}, u_{CBR}^{C}.*

5. Conclusion

In this paper, an improved hybrid HVDC transmission system based on diode rectifier units and full-bridge MMC is proposed and analyzed for integration and transmission of large-scale offshore wind farms. The active power-DC voltage droop control strategy is proposed and the analytical model of FB-MMC control loop is established to balance the active power of DRUs and FB-MMC by dynamically modifying the droop coefficient. The reactive power control strategy is able to dynamically balance total reactive power of wind farm, DRUs and FB-MMC under wind farm power variations and after occurrence of DC pole-to-pole short circuit fault and offshore POI bus solid fault. By the reverse and double DC voltage of FB-MMC when blocked, the short circuit current is limited to a lower level for semiconductor devices and cables as soon as possible. Meanwhile, the wind farm can be precharged by FB-MMC before starting transmission. The overall configuration and control is verified in PSCAD/EMTDC and the simulation results agree well with theoretical analysis. Therefore, the scheme in this paper is a promising solution for large-scale offshore wind power transmission.

6. Acknowledgments

This work is supported by National Key R&D Program of China under Grant 2017YFB0903100 and by Science and Technology Project of State Grid Corporation of China under Grant 521104170043.

7. References

[1] https://public.tableau.com/views/IRENARETimeSeries/Charts?:embed=y&:showVizHome=no&publish=yes&:toolbar=no

[2] 'Global Wind Report 2021', https://gwec.net/global-wind-report-2021/

[3] The China Electric Power Research Institute.: 'UHV Transmission Technology' (ACADEMIC PRESS, 2017, 1st ed.).

[4] Lesnicar, A., Marquardt R.: 'An innovative modular multilevel converter topology suitable for a wide power range', IEEE PowerTech. Conf., Bologna, Italy, Jun. 23–26, 2003, vol. 3.

[5] Perez, M. A., Bernet S., Rodriguez J., Kouro S., Lizana R.: 'Circuit topologies, modeling, control schemes, and applications of modular multilevel converters', IEEE Trans. Power Electron., 2015, 30(1), pp. 4-17.

[6] Dekka A., Wu B., Fuentes R. L., Perez M., Zargari N. R.: 'Evolution of topologies, modeling, control schemes, and applications of modular multilevel converters', IEEE J. Emerg. Sel. Topics Power Electron., 2017, 5(4), pp. 1631-1656.

[7] Guan M., Xu Z., Pan W., Tu Q.: 'Analytical calculation of fundamental wave and harmonic characteristics for nearest level modulation', High Voltage Engineering, 2010, 36(5), pp. 1327-1332.

[8] Li B., Yang R., Xu D., Wang G., Wang W., Xu D.: 'Analysis of the phase-shifted carrier modulation for modular multilevel converters', IEEE Trans. Power Electron., 2015, 30(1), pp. 297-310.

[9] Leon J. I., Kouro S., Franquelo L. G., Rodriguez J., Wu B.: 'The essential role and the continuous evolution of modulation techniques for voltage-source inverters in the past, present, and future power electronics', IEEE Trans. Ind. Electron., 2016, 63(5), pp. 2688-2701.

[10] Liu Q., Chen A., Du C., Zhang C.: 'A modified nearest-level modulation method for modular multilevel converter with fewer submodules', 2017 Chinese Automation Congress (CAC), Jinan, 2017, pp. 6551-6556.

[11] Thakur S. S., Odavic M., Allu A., Zhu Z. Q., Atallah K.: 'Theoretical Harmonic Spectra of PWM Waveforms Including DC Bus Voltage Ripple—Application to a Low-Capacitance Modular Multilevel Converter', IEEE Trans. Power Electron., 2020, 35(9), pp. 9291-9305.

[12] Li Y., Shi X., Liu B., Wang F., Lei W.: 'Maximum modulation index for modular multilevel converter with circulating current control', Proc. IEEE Energy Convers. Congr. Expo., 2014, pp. 491–498.

[13] Angquist L., Antonopoulos A., Siemaszko D., Ilves K., Vasiladiotis M., Nee H.: 'Open-loop control of modular multilevel converters using estimation of stored energy', IEEE Trans. Ind. Appl., 2011, 47(6), pp. 2516-2524.

[14] Peralta J., Saad H., Dennetiere S., Mahseredjian J., Nguefeu S.: 'Detailed and Averaged Models for a 401-Level MMC–HVDC System', IEEE Trans. Power Del., 2012, 27(3), pp. 1501–1508.

[15] Innodc.org. 2021.: 'Connection of offshore wind farms – Innovative tools for offshore wind and direct current (DC) grids', https://innodc.org/connection-of-offshore-wind-farms/

[16] 'ABB review', https://lIbrary.e.abb.com/public/fc940515a6834d018f38bbea148e5ec3/ABB%20Review%20High%20Voltage%20special%20report.pdf?xsign=wjMYOtjZ0yPQBoymdUSo9PIA8zEv2ei28TG2QbIOIAbWGfBKIEflXepfyaN8uq7v

[17] Pan E, Yue B, Li X, Zhao Z, Zhu Q.: 'Integration technology and practice for long-distance offshore wind power in China', Energy Convers Econ. 2020, 1(1), pp. 4–19.

[18] Li Z, Song Q, An F, Zhao B, Yu Z, Zeng R.: 'Review on DC transmission systems for integrating large-scale offshore wind farms', Energy Convers Econ. 2020, 2(1), pp. 1–14.

[19] Van, H.D., Gomis-Bellmunt O., Liang J.: 'Wind turbine technologies', in 'HVDC Grids: For Offshore and Supergrid of the Future' (IEEE press, 2016, 1st ed), pp. 97–108.

[20] Kuhn O., Menke P., Zurowski R., Christ T., Seman S., Giering G.: '2nd generation DC grid access for offshore wind farms: HVDC in an AC fashion', Proc. CIGRE, Paris, France, 2016, pp. 1–7.

[21] Yu L., Li R., Xu L. Adam G. P.: 'Analysis and Control of Offshore Wind Farms Connected with Diode Rectifier-Based HVDC System', IEEE Trans. Power Del., 2020, 35(4), pp. 2049-2059.

[22] Yu L., Li R., Xu L.: 'Distributed PLL-Based Control of Offshore Wind Turbines Connected with Diode-Rectifier-Based HVDC Systems', IEEE Trans. Power Del., 2018, 33(3), pp. 1328-1336.

[23] Blasco-Gimenez R., Añó-Villalba S., J. Rodrguez-D'Derlée F. Morant, Bernal-Perez S.: 'Distributed Voltage and Frequency Control of Offshore Wind Farms Connected with a Diode-Based HVdc Link', IEEE Trans. Power Electron., 2010, 25(12), pp. 3095-3105.

[24] Bernal-Perez S., Añó-Villalba S., Blasco-Gimenez R., Rodriguez-D'Derlée J.: 'Off-shore wind farm grid connection using a novel diode-rectifier and VSC-inverter based HVDC transmission link', IECON 2011-37th Annual Conference on IEEE Industrial Electronics Society, 2011, pp. 3186-3191.

[25] Sao C. K., Lehn P. W.: 'Control and Power Management of Converter Fed Microgrids', IEEE Trans. Power Syst., 2008, 23(3), pp. 1088–1098.

[26] Prignitz C., Eckel H. G., Achenbach S., Augsburger F., Schön A.: 'FixReF: A control strategy for offshore wind farms with different wind turbine types and diode rectifier HVDC transmission', 2016 IEEE 7th International Symposium on Power Electronics for Distributed Generation Systems (PEDG), 2016, pp.1-7.

[27] Li R., Xu L.: 'A Unidirectional Hybrid HVDC Transmission System Based on Diode Rectifier and Full-Bridge MMC', IEEE J. Emerg. Sel. Topics Power Electron., 2021, 9(6), pp. 6974-6984.

[28] Li R., Yu L., Xu L., Adam G. P.: 'DC Fault Protection of Diode Rectifier Unit Based HVDC System Connecting Offshore Wind Farms', 2018 IEEE Power & Energy Society General Meeting (PESGM), Portland, OR, USA. Aug. 2018, pp. 1-5.